scientific reports

Check for updates

OPEN

Organic molecule functionalized lead sulfide hybrid system for energy storage and field dependent polarization performances

Sarit K. Ghosh[1], Ibrahim Waziri[1], Maolin Bo[2], Harishchandra Singh[3], Rafique Ul Islam[4] & Kaushik Mallick[1]✉

A wet chemical route is reported for synthesising organic molecule stabilized lead sulfide nanoparticles. The dielectric capacitance, energy storage performances and field-driven polarization of the organic–inorganic hybrid system are investigated in the form of a device under varying temperature and frequency conditions. The structural analysis confirmed the formation of the monoclinic phase of lead sulfide within the organic network. The band structure of lead sulfide was obtained by density functional theory calculation that supported the semiconductor nature of the material with a direct band gap of 2.27 eV. The dielectric performance of the lead sulfide originated due to the dipolar and the space charge polarization. The energy storage ability of the material was investigated under DC-bias conditions, and the device exhibited the power density values 30 W/g and 340 W/g at 100 Hz and 10 kHz, respectively. The electric field-induced polarization study exhibited a fatigue-free behaviour of the device for 10^3 cycles with a stable dielectric strength. The study revealed that the lead sulfide-based system has potential in energy storage applications.

Semiconductor nanoparticles have attracted much attention because of their interesting electrical and optical properties, originating from quantum confinement effect[1]. Among the various semiconductor nanomaterials, metal sulphides have received much attention due to their appropriate electronic band gap and bandposition[2]. So far as application point of view, metal sulfides based devices displayed efficient performances in several areas including fuel cell[3], solar cell[4], light-emitting diode[5], gas sensor[6], battery[7], supercapacitor[8], thermoelectric[9], dielectric[10] and memory[11] applications.The performance of the devices predominantly depends on the nano architecture of the metal sulfides.

In this context, lead sulfide, a binary (IV–VI) semiconductor material, with moderately small bandgap and large exciton Bohr radius (18 nm), stand out as promising material that has been successfully used for different applications such as infrared sensors[12], solar cells[13], light-emitting diodes[14], lasers[15] and biological imaging[16] due to its controllable size with variety of morphologies. Different morphologies, such as rod and cube[17], spherical and dendritic[18], wire[19], and star[20] shaped lead sulfide has been reported, at nanometer to micrometer scale, by several synthetic methods, such as, microwave, hydrothermal, solvothermal, and chemical or thermal decomposition, under different reaction conditions (precursor varities, temperature, time, solvent and stabillizer)[17,21,22].

Nanocrystalline lead sulfide also exhibited the catalytic performance for the synthesis of amidoalkyl-naphthols under solvent-free conditions[23] and for the chemical reduction of *p*-nitroaniline[24]. The narrow bandgap, high electron mobility and excellent chemical stability enable the lead sulfide as a promising photocatalytic material[25]. The lead sulfide nanoparticle initiated photocatalytic degradation of bromothymol blue has been reported due to electron–hole pair generation mechanism[26].

[1]Department of Chemical Sciences, University of Johannesburg, P.O. Box: 524, Auckland Park 2006, South Africa. [2]Key Laboratory of Extraordinary Bond Engineering and Advanced Materials Technology (EBEAM) of Chongqing, Yangtze Normal University, Chongqing 408100, China. [3]Nano and Molecular Systems Research Unit, University of Oulu, 90014 Oulu, Finland. [4]Department of Chemistry, School of Physical Sciences, Mahatma Gandhi Central University, Motihari 845401, India. ✉email: kaushikm@uj.ac.za

Material type	Synthesis method	Crystal structure	Electrical and physical properties	References
PbS nanocrystal	Solvothermal route	Cubic	Solar energy storage	[55]
Nanocrystal and nanocomposite of PbS	Ligand exchange and chemical synthesis route	–	Photoluminescent property and photovoltaic application	[56,57]
PbS nanocrystal	ligands mediated synthesis and chemical route	Cubic	Photovoltaic and photoluminescent property	[58,59]
PbS nanoplatelets	Chemical route	Orthorhombic	Morphology, band structure	[42]
Nanocomposite of PbS-graphene	Hydrothermal	Cubic	Gas sensor	[60]
PbS nanosheet	Colloidal synthesis route	Orthorhombic	Photoconductivity, optical absorption, band structure	[61]
PbS nanocrystal	Ligand based complexation	Cubic	$\varepsilon' \sim 13.4$	[31]
Thin film of PbS	Chemical bath deposition	Cubic	$\varepsilon' \sim 155–265$	[32]
Sr-doped PbS	Microwave route	Cubic	$\varepsilon' \sim 25–57$, AC-conductivity	[33]
Ce-doped PbS	Chemical route	Cubic	$\varepsilon' \sim 17.5–25$, DC-conductivity	[34]
Aniline and 4-fluoroaniline stabilized PbS nanocrystal	Ligand based complexation	Monoclinic	$\varepsilon' \sim 376$ (ALS) $\varepsilon' \sim 800$ (FALS) @ 100 Hz and 30 °C, AC-conductivity, energy and power density, polarization loop	Present work

Table 1. The synthesis methodology, structure and physical properties of some of the reported lead sulfide based system.

Employing the band gap engineering, using different ligands, the electrical property of lead sulfide based field-effect transistor showed the transformation from ambipolar to strong n-type behaviour[27]. The colloidal lead sulfide quantum dots also contribute to the improvement of solar cell efficiencies through better carrier extraction[28]. The dopped lead sulfide nanocrystal experienced an improvement of optical properties due to charge injection[29]. Optical properties of lead sulfide, based on theoretical calculation, exhibited good reflection and absorption for ultraviolet electromagnetic waves, suggested a potential candidate for photoconductive devices in ultraviolet range[30]. Lead sulfide exhibited immense potential in microelectronics application. The lead sulfide nanocrystal, with cubic symmetry, exhibited low dielectric constant and dielectric loss over a wide range of temperature and frequency conditions[31]. Nanoparticles of lead sulfide grown within the pores of polyvinyl alcohol matrix exhibited the moderate value of dielectric constant at higher frequencies[32]. It has been reported that lead sulfide nanoparticles, doped with strontium[33] or cerium[34], displayed an improved dielectric and electrical characteristics, compared to the pure lead sulfide. Two dimensional cubic phase lead sulphide nanosheets, synthesized using solid state reaction method, exhibited high values of dielectric constant and have potential as capacitive storage device[35].

Lead sulfide with cubic structure is common in literature, Table 1, however the formation of monoclinic lead sulfide is relatively rare[36–38]. In this study, a complexation mediated wet chemical route was applied for the synthesis of fluoroaniline stabilized monoclinic lead sulfide nanoparticles. The dielectric capacitance, energy density, AC-conductivity and field driven polarization performances of the synthesized material was investigated in form of a device under varying temperature and frequency conditions. A comparative study was also performed on the device based on aniline stabilized lead sulfide system. A mechanism based on the performances of the two devices is also discussed in this manuscript.

Result and discussion

A complexation mediated route was applied for the preparation of lead sulfide nanoparticles, where 4-fluoroaniline was served the role of a ligand and also as a stabilizer of the particles. The detail NMR characterization of the ligand and products are available in the supporting information (Table S1 and Figs. S1, S2). The TEM images, Fig. 1A,B, with different magnifications, of the fluoroaniline stabilized lead sulfide displayed the spherical shaped lead sulfide particles (dark spots) within the size range of 8–12 nm, presented using a histogram, Fig. 1A, inset. The selected area electron diffraction (SAED) pattern of lead sulfide displayed in Fig. 1B, inset, obtained from the groups of particles.

The X-Ray diffraction pattern of lead sulfide nanoparticles was recorded within the range (2θ) from 20° to 80°, Fig. 2A. The overall diffraction pattern was matched according to the ICSD: 68712, which belongs to the monoclinic phase of lead sulfide with the space group of P1. The monoclinic structure, with the lattice constant values, $a = 6.00$ Å, $b = 6.02$ Å, $c = 22.43$ Å and $\alpha = \gamma = 90°$, $\beta = 95.4°$, accompanied with a large unit cell volume of 808.54 Å^3. Figure 2A, inset, represents the three dimensional unit cell structure of lead sulfide, elongated along the c-axis. In lead sulfide, with the atomic arrangement of lead and sulphur along the 8-asymmetrical lattice sites in the structure[36–38]. The details positional coordinates of lead sulfide system is mentioned in Table S2, supporting information.

The local structure of lead sulfide (PbS) nanoparticles was investigated using Raman spectroscopy technique. The Raman spectrum (Fig. 2B), was deconvoluted (green colour peaks) into nine Raman active vibrational modes, from ν_1 to ν_9, within the range from 40 to 900 cm^{-1}. The spectrum consists of strong intensity vibrational modes (ν_1 and ν_2), diffuse modes (ν_3, ν_4, ν_5 and ν_8) and broad intensity modes (ν_6, ν_7 and ν_9). Raman active modes positioned at $\nu_1 \sim 81$ cm^{-1} and $\nu_2 \sim 137$ cm^{-1} along with a shoulder like feature at $\nu_3 \sim 184$ cm^{-1}, originated from the longitudinal optical phonon vibration of Pb–S phase[39]. The diffuse modes $\nu_4 \sim 216$ cm^{-1} and $\nu_5 \sim 254$ cm^{-1} are associated to the symmetrical vibration of nonlinear S-Pb–S chain and the radial vibration of the of $(PbS)_n$

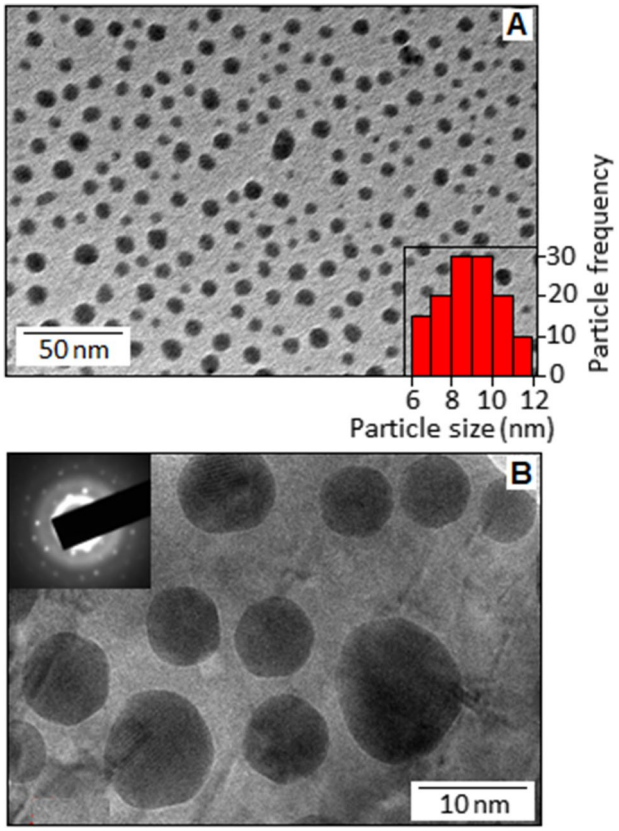

Figure 1. The transmission electron microscope images of the fluoroaniline stabilized lead sulfide nanoparticles with different magnifications (**A**, **B**). The inset image in (**A**) represent the size distribution of the particles and the inset image in (**B**) is the selected area electron diffraction pattern of lead sulfide.

cluster, ($n = 1–9$), respectively, in the monoclinic structure[40]. The broad peak at $\nu_6 \sim 328$ cm^{-1}, combined with smaller peaks at $\nu_7 \sim 410$ cm^{-1} and at $\nu_8 \sim 470$ cm^{-1}, related to the various stretching modes of S–S bond in the structure[41]. The vibrational mode observed at $\nu_9 \sim 546$ cm^{-1} correspond to the phononic replicas of Pb–S phase[39].

Figure 3A,B show the distribution of local density of states (LDOS) of lead sulfide. The structure illustrated the *s* and *p*-orbital contribution in the density of states (Fig. 3A) and the atomic density of states of Pb and S (Fig. 3B). The effective distribution of the states concluded that the valance band edge has *p*-orbital like character and typically localized with the S-atom, whereas the Pb-atom contribute more towards conduction band[42]. The band structure of lead sulfide was obtained by density functional theory calculation (Fig. 3C), that supported the semiconductor nature of the material with a direct band gap of 2.27 eV. Figure 3D represents the deformation charge density of the lead sulfide structure. The blue part represents the gain of electrons (electron population), and the red part symbolizes the loss of electrons (electron reduction).

The qualitative analysis of the chemical states of the fluoroaniline stabilized lead sulfide nanocrystal was explored by X-ray photoelectron spectroscopy (XPS) technique. The survey spectrum (Fig. 4A), exhibited the presence of elemental peaks of C, N, O, F, S and Pb. The N (1 s) and O (1 s) peaks are positioned at 399.5 and 529.8 eV, respectively. The carbon, nitrogen and fluorine signals are originated from the organic matrix (fluoroaniline) and the O (1 s) signal is developed due to the surface oxidation of the sample. The binding energy peaks originated from the Pb $5d_{5/2}$, Pb 4f, Pb $4d_{5/2}$, Pb $4d_{3/2}$, and Pb $4p_{3/2}$ are also visible in the survey spectrum[43]. The high resolution Pb 4f spectrum (Fig. 4B) shows spin–orbit splitting of Pb ($4f_{7/2}$) and Pb ($4f_{5/2}$) with the peaks positioned at 139.1 eV and 143.8 eV, respectively, associated with the lead sulfide component[44].

The deconvoluted of Pb 4f doublet peaks also display two additional small peaks positioned at 138.1 eV and 143.1 eV, originated from the surface oxidation of lead sulfide with the formation of lead sulfite ($PbSO_3$) like species, under the exposure of aerial oxygen[44]. The high resolution S 2p core level spectrum, after deconvolution, Fig. 4C shows two peaks located at 161.5 eV and 162.7 eV, correspond to S ($2p_{3//2}$) and S ($2p_{1//2}$), for the sulfide ion of lead sulfide[44]. The formation of lead sulfite species, due to the surface oxidation of lead sulfide, was also evidenced in the spectrum, with the binding energy values positioned at 163.3 eV and 167.7 eV, also reported in other lead sulfide systems[44]. The values of the binding energy were calibrated utilizing C 1 s peak at 285.1 eV, as the internal standard, associated with the carbon from the aromatic ring (Fig. 4D). Other C 1 s peak with the binding energy value of 286.6 eV related to -C-F interaction form fluoroaniline[45]. Further, after deconvolution of the F1s spectra (Fig. 4E), two peaks are developed. The peak with the binding energy value of 689.6 eV is originated from the fluorine in fluoroaniline molecule and the other peak at 687.5 eV associated with lead-fluorine interaction from the neighbouring fluoroaniline molecule.

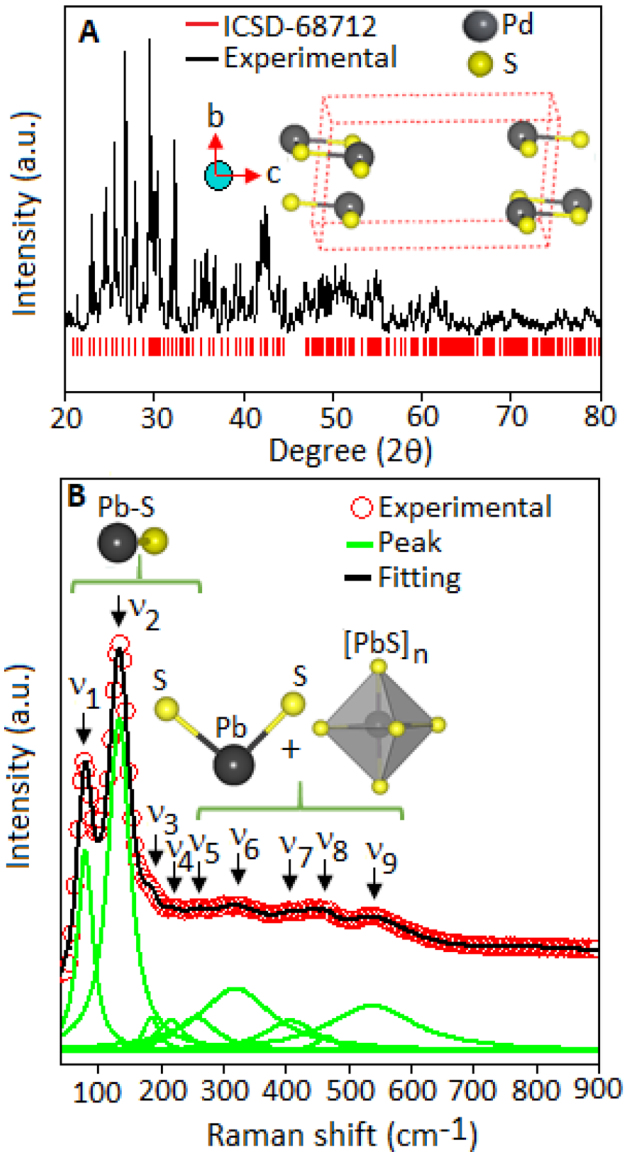

Figure 2. (**A**) X-ray diffraction pattern of lead sulfide (black line) was measured within the range of 20–80°. The diffraction pattern was indexed according to ICSD: 68712 (red colour bar) of the monoclinic structure. The inset figure shows the unit cell of lead sulfide projected along a-axis. (**B**) The deconvoluted Raman spectrum (green colour), within the range from 40 to 900 cm^{-1}, with Raman active vibrational modes (ν_1–ν_9).

Figure 5A shows the temperature (from 30 to 120 °C) and frequency (from 100 Hz to 1 MHz) dependent dielectric constant (ε′) of FALS based device. At 30 °C, the value of dielectric constant (ε′) ~ 800 was achieved under the frequency condition of 100 Hz. With increasing the frequency, the dielectric constant decreased gradually and attained a stable value of ε′ ~ 360 at 1 MHz. At 120 °C, a substantial rise of the value of dielectric constant (ε′) ~ 2000 was observed at the frequency of 100 Hz, which was also decreased gradually towards higher frequencies. The capacitive behaviour of the lead sulfide was associated to the dipolar type of polarization. The dipoles are formed due to the separation of bound charges in the form of Pb^{2+} cation and S^{2-} anion, under the applied electric field. The structural analysis showed the deformation of charge density in the lead sulfide system and the charge transfer is directed towards the high electronegative sulphur atom. This kind of charge separation caused the formation of dipole moments. At lower frequency region, the induced dipoles are effectively followed with the applied field and attained a maximum value of dielectric constant. With increasing frequency, the dipoles are not able to respond with the field direction, which caused the decrease of dielectric constant values. The capacitive behaviour of the FALS based device was associated with the dipolar type of polarization (originated from the lead sulfide and highly polarised fluoroaniline molecule) and the space charge or interfacial polarization. The hydrogen atom of $-NH_2$ group in fluoroaniline forms intermolecular hydrogen bond with the neighbouring fluorine of fluoroaniline, resulted high negative charge density (Scheme 1). This interface creates space charge within the system, which prompted further increase of dielectric constant value. In addition to that, the defect

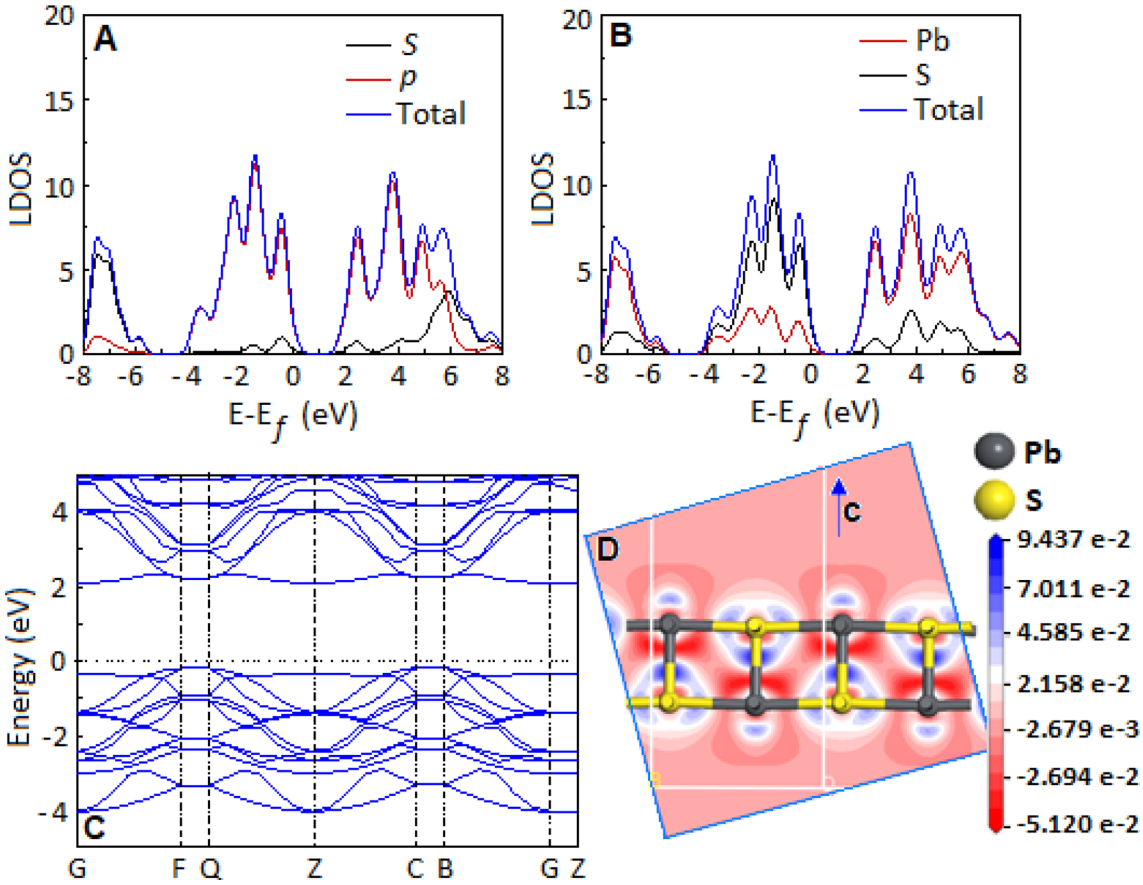

Figure 3. The distribution of local density of states of the lead sulfide. (**A**) The *s* and *p* orbital density of states and (**B**) the atomic, Pb and S, density of states. (**C**) Band structure of lead sulfide. (**D**) Deformation charge density of lead sulfide. (The Cambridge Sequential Total Energy Package, CASTEP, was used to optimize the geometry and calculating local charge and electronic properties, Supplementry information).

site of the nanoparticles and the organic–inorganic interface create the space charge within the system[10,46,47]. The space charge polarization is predominant towards the lower frequency range. The temperature effect on the dielectric constant of the device was associated with the loss factor of the material, as evidenced from the tan δ curve (Fig. 5A, inset). The rise in the tan δ curve with increasing the temperature implies that the space charges are thermally activated under the longer response time.

The dielectric polarization of the device was further analysed in term of capacitance as a function of frequency, under a series of voltage conditions (from 20 to 100 V) (Fig. 5B). From the figure it is evident that at lower frequency and lower voltage the change of capacitance is more favourable. At low voltage condition the polarization of the dipoles become facile. With increasing external voltage, the dipoles of the lead sulfide are aligned along the field direction with a restriction of the reversible polarization that resulted the decrease of capacitance value. Figure 5C exhibited the graphical representation of the inverse of capacitance ($1/C^2$) as a function of voltage (V) under the frequency condition of 500 Hz, 10 kHz, 100 kHz and 1 MHz. The slope of the plots suggests that the negative charge carriers are dominant in the lead sulfide system[27,28]. The variation of carrier density (N_D) and barrier potential (ϕ_B) with respect to the frequency is plotted in the Fig. 5D,E, respectively. The increasing value of carrier density with frequency originated from the localized electronic state of the material with decreasing the value of barrier potential[48,49]. The dipolar contribution, originated from the bound charges of lead-sulfide system, is responsible for the localized deformation of electronic structure under applied frequency conditions.

The maximum energy storage density (E_{max}) of the FALS based device was calculated under different DC-bias condition using the equation, $E_{max} = \frac{1}{2}CV_M^2$, where C represent the DC capacitance and V_M is the applied voltage. The E_{max} value of ~ 0.10 mJ/g was achieved at 100 V (under 100 Hz frequency condition) and the E_{max} values decreased with increasing frequency (Fig. 6A). The variation of E_{max} is more prominent towards lower frequencies (below 1 kHz) under high voltage condition (Fig. 6B). The equivalent series resistance (ESR) of the device was extracted from AC-impedance measurement, which exposed an insignificant variation under different bias conditions (Fig. 6C) (in log–log scale). The circuit representation of the device Fig. 6D), can be sketched by assuming that the stored energy was discharged through a load resistance (R_{load}), connected in parallel with a capacitor (C) and a resistor (R). The product of capacitance and resistance is the time constant (t) and the ratio of energy density to time constant (RC) gives the power density, which is a gravimetric power density that determine the minimum time required to discharge the stored energy of the device. The maximum power (P_{max}) delivered to the load resistance can be expressed as $P_{max} = E_{max}/2RC$. The calculated RC values were obtained 1.5 ms and

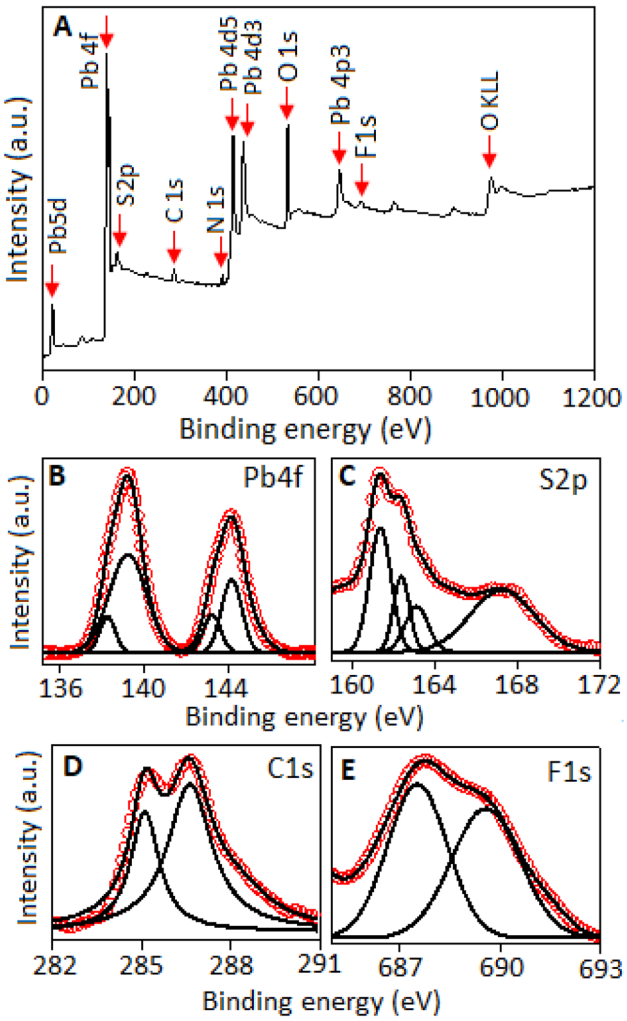

Figure 4. (**A**) The XPS survey spectrum of fluoroaniline stabilized lead sulfide. High-resolution XPS spectrum of (**B**) Pb 4f, (**C**) S 2p, (**D**) C1s and (**E**) F1s.

16 µs with the gravimetric power density values of 30 W/g and 340 W/g, at 100 Hz and 10 kHz, respectively, for the lead sulfide based device. A table of comparison based on the previously published results on gravimetric power density values for other organic–inorganic hybrid systems is mentioned in the supporting information, Table S3, as a ready reference.

The mobility of the charge carrier of the FALS based device was analysed in terms of AC-conductivity as a function of frequency for 30, 80 and 120 °C (Fig. 7A). Figure shows that the AC-conductivity is directly proportional to the applied frequency and also with the temperature. At 100 Hz, the conductivity values are 2.1×10^{-4} $S.m^{-1}$ and 2.3×10^{-3} $S.m^{-1}$ at 30 and 120 °C, respectively. The conductivity curves, for each temperature, has two regions, designated as region (I) and region (II), marked in the Fig. 7A. All the conductivity curves are finally merged towards the region (II). The region (I) exhibits a slow progress of conductivity with increasing frequency, on the other hand, the conductivity increases sharply with increasing the frequency, in the region (II). The conductivity behaviour was analysed in term of Jonscher's universal power law,$\sigma_{ac} = \sigma_{dc} + A(T)\omega^S$, where, σ_{dc} is the DC-part of the conductivity, A is the temperature dependent coefficient of the system and S is the temperature dependent parameter that determine the conduction mechanism of the charge carriers. In the low frequency region (I), the slow progress of conductivity with frequency, indicates few trapped charges are available for the conduction process, whereas the region (II) specify that large number of trapped charges are available in the conduction process. Several models have been proposed to study the conduction mechanism of the charge carriers[50]. It is reported that the polaron and bipolaron types of charge carriers are responsible for conduction mechanism in hybrid material[51]. The hybrid system of metal sulfides and metal halides demonstrated the formation of polaronic charge species that control the hopping and tunnelling type of transport mechanism[47,52]. The conductivity curves were fitted using Jonscher's power law for the regions (I) and (II) (Fig. 7A, red line), and the extracted $S_{(I)}$ and $S_{(II)}$ parameters were plotted in Fig. 7A, inset. The values of $S_{(I)}$ and $S_{(II)}$ are decrease with increasing temperature, suggested the hopping conduction of polaron was involved in the lead sulfide based device system. The variation of AC-conductivity (σ_{AC}) with temperature (1/T), described by Arrhenius equation, $\sigma_{AC}(T) = \sigma_0 \exp(-E_a/K_B T)$, σ_0 is pre-exponential factor and E_a is activation energy, was measured at the

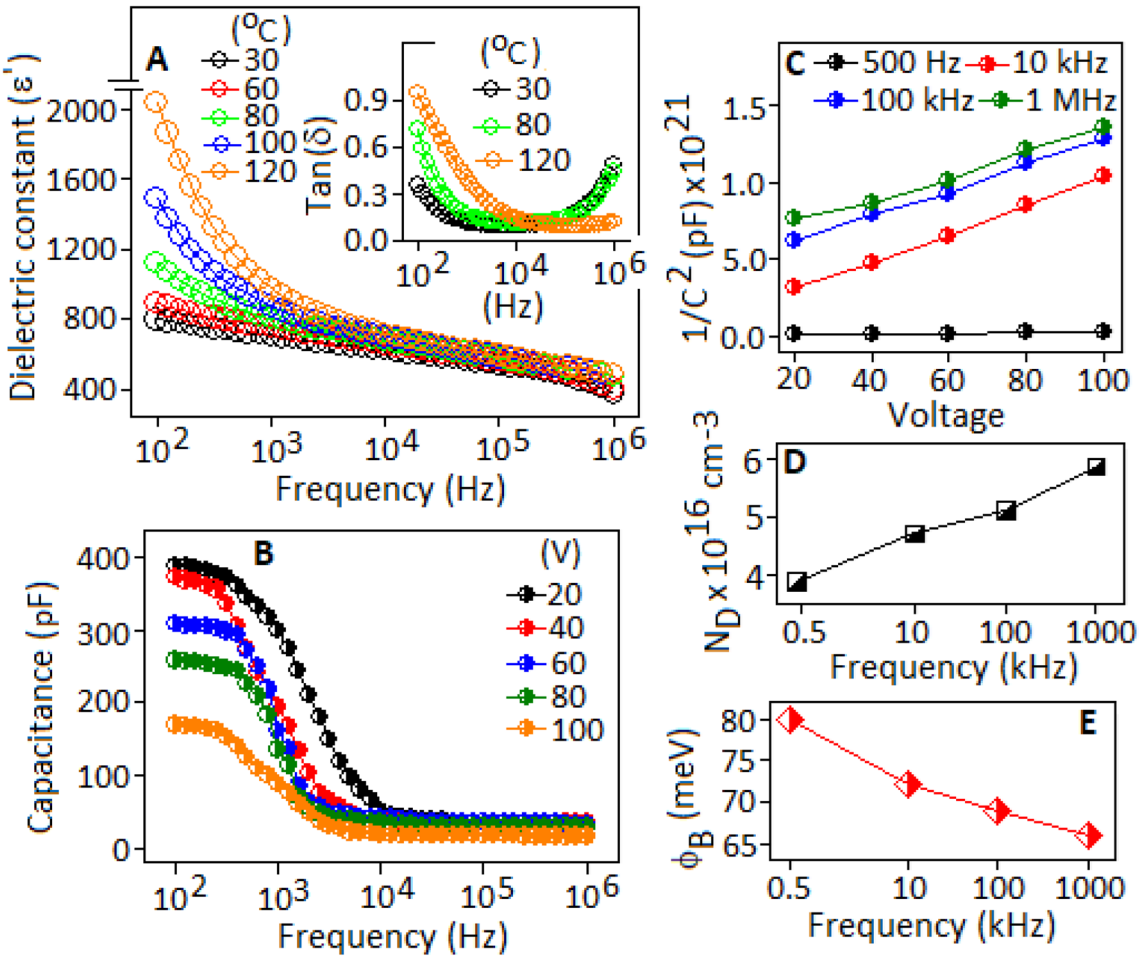

Figure 5. (**A**) Dielectric constant (ε′) of FALS based device measured at 30, 60, 80, 100 and 120 °C under the frequency range from 100 Hz to 1 MHz. The variation of tan δ curves for selected temperatures, inset. (**B**) Graphical representation of capacitance as a function of frequency under applied voltage conditions. (**C**) $1/C^2$–V plot under selected frequency conditions. (**D**) and (**C**) represent the variation of carrier concentration (N_D) and barrier potential (ϕ_B) as a function of frequency, for FALS based device.

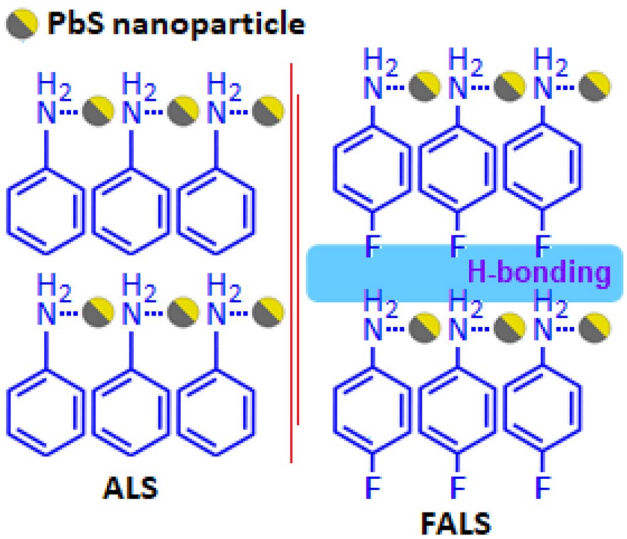

Scheme 1. The schematic diagram of aniline and fluoroaniline stabilized lead sulfide nanoparticles. Hydrogen bond formation in fluoroaniline stabilized lead sulfide system.

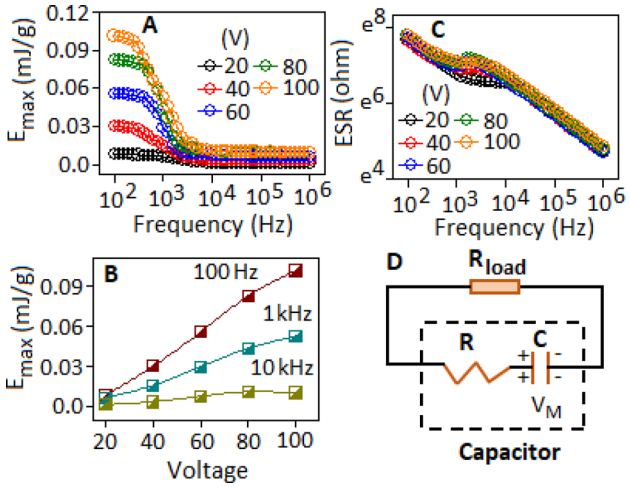

Figure 6. (**A**) Variation of energy density (E_{max}) with respect to frequency, under DC-voltage, (**B**) energy density (E_{max}) as a function of voltages under different frequency condition, (**C**) equivalent series resistance (ESR) as a function of frequency under different voltage condition (in log–log scale), (**D**) equivalent circuit representation for the energy and power transfer model at a certain voltage (V_M), for the FALS based device.

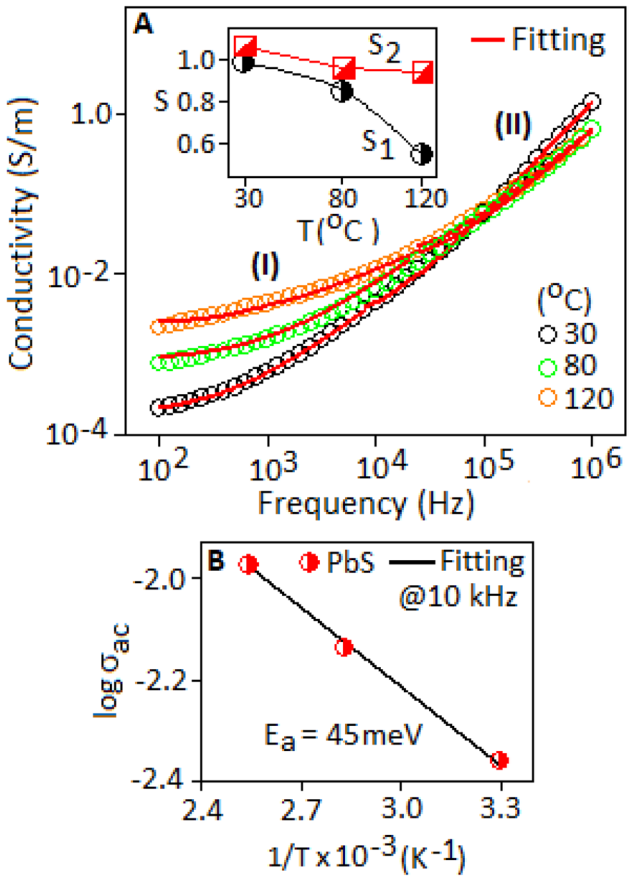

Figure 7. (**A**) AC-conductivity behaviour of the FALS based device at 30, 80 and 120 °C, measured under the frequency range from 100 Hz to 1 MHz (fitting was done according to the Jonscher's power law, red line). The inset figure shows the variation of S_1 and S_2 parameters, extracted from the region (I) and (II), respectively. (**B**) Arrhenius plot of AC-conductivity as a function of inverse temperature (1/T), at 10 kHz.

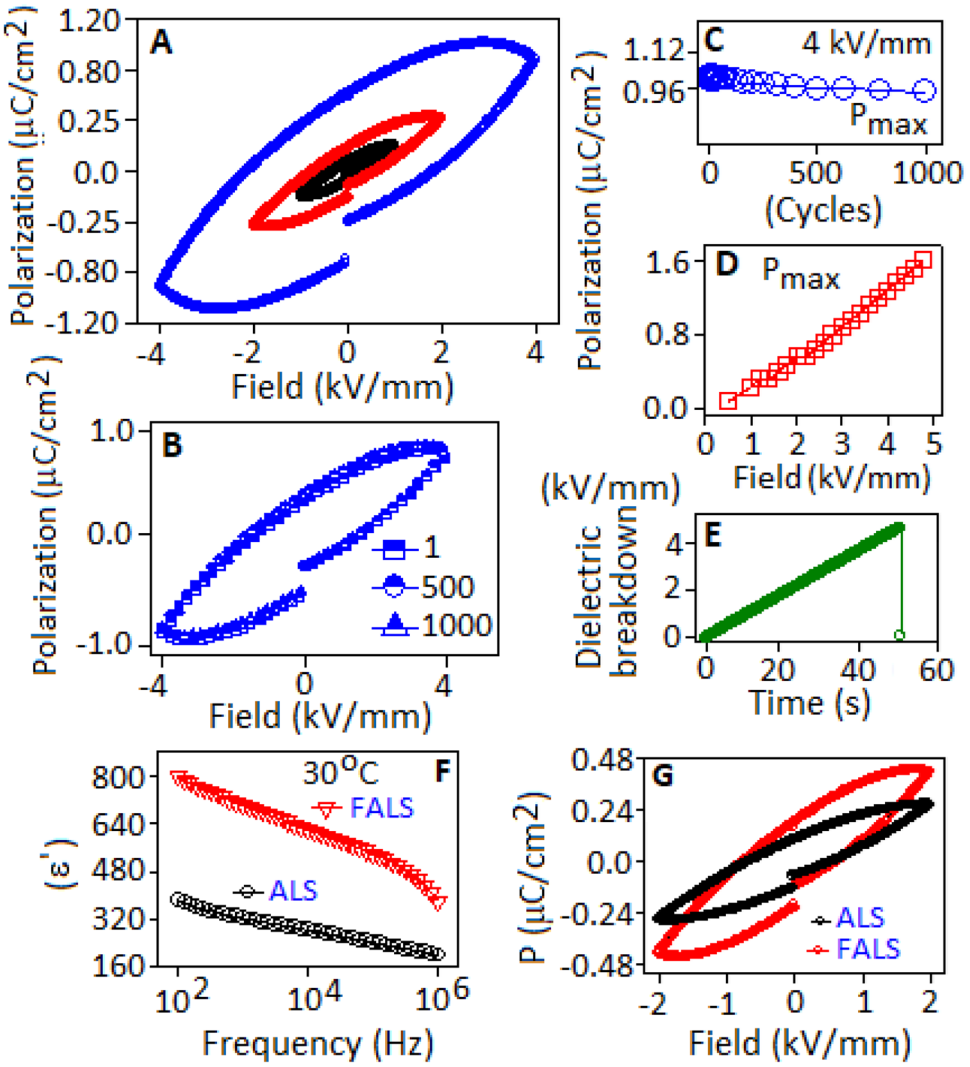

Figure 8. (**A**) Hysteresis loop, polarization vs electric field, of the FALS based device, measured at 100 Hz. (**B**) Hysteresis loop of the device under 4 kV/mm field condition, for 10^3 cycles. (**C**) Endurance behaviour of the device (in terms of maximum polarization, P_{max}) for 1000 cycles, at 4 kV/mm. (**D**) Increment of maximum polarization (P_{max}) values with respect to the applied electric field. (**E**) Dielectric breakdown strength (kV/mm) of the device as a function of time, measured at a scan rate of 200 V/s. Variation of (**F**) dielectric constant (ε′) and (**G**) polarization vs electric field, hysteresis loop of ALS and FALS based device.

frequency of 10 kHz. The E_a value was obtained ~ 45 meV, extracted from the linear fit of the equation (Fig. 7B). The small E_a value recommended the polaron mediated conduction within the system[53].

Figure 8A shows the polarization–electric field (P–E) hysteresis loop for the FALS based device, measured under 1, 2 and 4 kV/mm, field conditions. The dipolar type of polarizability of lead sulfide was responsible for the formation of hysteresis loop. The unsaturated pattern of the loops was associated with the space charge contribution in the system[54]. A steady polarization hysteresis loop was observed for the device at ± 4 kV/mm (Fig. 8B), and maintained the maximum polarization value within the range from 1.1 to 0.99 μC/cm^2 for 10^3 cycles (Fig. 8C). The polarizability of the covalent bond of the lead sulfide system was increased with increasing applied electric field and reached to the maximum polarization (P_{max}) value of 1.6 μC/cm^2 at 5 kV/mm (Fig. 8D). The dielectric breakdown strength of the device exhibited the tolerance up to 5.2 kV/mm of electric field, without any electrical breakdown and above that field the device experienced an electrical breakdown after 50 s (Fig. 8E).

A comparative study was performed between aniline and fluoroaniline stabilized lead sulfide based devices to investigate the role of fluorine. A similar synthesis method, like FALS, was applied for the preparation of aniline stabilized lead sulfide nanoparticles (ALS).

The aniline stabilized lead sulfide (ALS) and fluoroaniline stabilized lead sulfide (FALS) exhibited the dielectric constant values (ε′) ~ 376 and ~ 800, respectively, at 30 °C under 100 Hz frequency condition (Fig. 8F). The graphical representation of polarization as a function of electric field exhibited the hysteresis loop with the maximum polarization values 0.29 and 0.46 μC/cm^2 for ALS and FALS based devices, respectively, at 2 kV/mm (Fig. 8G). High dielectric constant value of FALS was associated with the dipolar type of polarization and space

charge polarization. In FALS, the dipolar type of polarization was created from the lead sulfide and polarised fluoroaniline molecule, whereas in ALS only the dipoles of lead sulfide are responsible for polarization.

The hydrogen atom of the $-NH_2$ group forms intermolecular hydrogen bonding with the fluorine of FALS (Scheme 1) resulted high negative charge density. This interface procedures additional space charge in the system, which prompts further enhancement of the dielectric constant value in FALS based device. The increased area of the hysteresis loop and maximum polarization value of the FALS based device as compared with ALS based device were originated due to the above reasons.

Lead sulfide, with different size, shape and morphology, have been extensively investigated because of their unique optical and electronic properties, which endows the various potential applications. The electrical and physical properties of some reported lead sulfide based systems are mentioned in Table 1[31–34,42,55–61].

Conclusion

A complexation mediated wet chemical route was applied for the preparation of fluoroaniline stabilized monoclinic lead sulfide nanoparticles. The sizes of the synthesized particles are in the range of 8–12 nm, as evidenced from the microscopy analysis. The Raman spectrum analysis showed the different vibrational modes associated with lead sulfide. The X-ray photoelectron spectroscopy analysis confirmed the formation of lead (II) sulfide. The fluoroaniline stabilized lead sulfide based device exhibited the dielectric constant value of ~ 2000 at 120 °C at 100 Hz. The capacitive behaviour was associated with the dipolar type of polarization and the space charge polarization. The AC-conductivity values of the device were obtained 2.1×10^{-4} S m^{-1} and 2.3×10^{-3} S m^{-1} at 30 and 120 °C, respectively, at 100 Hz and the conductivity mechanism was followed by the hopping conduction of the polarons. The gravimetric power density values of 30 W/g and 340 W/g, at 100 Hz and 10 kHz, respectively, were achieved for the device. The device showed the maximum polarization value of 1.6 μC/cm^2 at 5 kV/mm. A quasi-stable maximum polarization value in the range of 1.1–0.99 μC/cm^2 was noted at 4 kV/mm, for 10^3 cycles. Based on the above mentioned performances we could assume that the device has the potential as a pulse capacitor in microelectronic application.

Experimental section

Materials. Analytical grade chemicals (lead nitride, sodium sulfide and *4*-fluoroaniline) were used in this study without further purification.

Synthesis of lead sulfide nanoparticles. In a typical experiment, 1.0 mL of *4*-fluoroaniline was diluted in 10 mL of methanol in a 50 mL conical flask. An aqueous solution of lead nitrate (10 mL) with the concentration of 0.1 mol dm^{-3} was added to the diluted *4*-fluoroaniline. A white precipitation of Pb(II)-fluoroaniline complex was formed immediately. To this precipitation, 5 mL of Na_2S solution (0.1 mol dm^{-3}) was added and instant change of colour of the precipitation in to black indicate the formation of fluoroaniline stabilized lead sulfide, FALS. The solid material was collected through filtration and dried under vacuum condition. The electrical properties of the synthesized materials were measured in the form of a device. The material characterization and device fabrication methods are available in the supporting information. The conditions set for computational analysis is also available in the supporting information.

Data availability

Data used for analyses in this manuscript are available from the corresponding author upon reasonable request.

Received: 26 May 2022; Accepted: 7 November 2022
Published online: 11 November 2022

References

1. Mehata, M., Majumder, M., Mallik, B. & Ohta, N. External electric field effects on optical property and excitation dynamics of capped CdS quantum dots embedded in a polymer film. *J. Phys. Chem. C* **114**, 15594–15601 (2010).
2. Chandrasekaran, S. *et al.* Recent advances in metal sulfides: from controlled fabrication to electrocatalytic, photocatalytic and photo electrochemical water splitting and beyond. *Chem. Soc. Rev.* **48**, 4178–4218 (2019).
3. Xiao, Y. & Tang, L. High throughput approach exploitation: Two-dimensional double-metal sulfide (M_2S_2) of efficient electrocatalysts for oxygen reduction reaction in fuel cells. *Energy Fuels* **34**, 5006–5015 (2020).
4. Dowland, S. *et al.* Direct growth of metal sulfide nanoparticle networks in solid-state polymer films for hybrid inorganic-organic solar cells. *Adv. Mater.* **23**, 2739–2744 (2011).
5. Song, W. & Yang, H. Efficient white-light-emitting diodes fabricated from highly fluorescent copper-indium-sulfide core/shell quantum dots. *Chem. Mater.* **24**, 1961–1967 (2012).
6. Tang, H. *et al.* Recent advances in 2D/nanostructured metal sulfide-based gas sensors: Mechanisms, applications, and perspectives. *J. Mater. Chem. A* **8**, 24943–24976 (2020).
7. Yan, B. *et al.* Design, synthesis, and application of metal sulfides for Li-S batteries: Progress and prospects. *J. Mater. Chem. A* **8**, 17848–17882 (2020).
8. Barik, R., Devi, N., Perla, V., Ghosh, S. & Mallick, K. Stannous sulfide nanoparticles for supercapacitor application. *Appl. Surf. Sci.* **472**, 112–117 (2019).
9. Chen, L. *et al.* Thermoelectric properties of polycrystalline palladium sulfide. *RSC Adv.* **8**, 13154–13158 (2018).
10. Ma, L., Ai, X., Yang, X., Song, X. & Wu, X. Dielectric and conductivity relaxation of rGO@CdS nanocomposites via in situ assembly of CdS nanoparticles on an rGO layer. *J. Phys. Chem. C* **124**, 25133–25141 (2020).
11. Perla, V., Ghosh, S. & Mallick, K. Transport mechanism of copper sulfide embedded carbon nitride thin film: A formation free memristor. *Mater. Adv.* **1**, 228–234 (2020).
12. Sun, Z. *et al.* Infrared photodetectors based on CVD-grown graphene and PbS quantum dots with ultrahigh responsivity. *Adv. Mater.* **24**, 5878–5883 (2012).

13. Chuang, C., Brown, P., Bulović, V. & Bawendi, M. Improved performance and stability in quantum dot solar cells through band alignment engineering. *Nat. Mater.* **13**, 796–801 (2014).
14. Navaneethan, M., Nisha, K., Ponnusamy, S. & Muthamizhchelvan, C. Optical, structural and surface morphological studies of *n*-methylaniline capped lead sulphide nanoparticles. *Rev. Adv. Mater. Sci.* **21**, 217–224 (2009).
15. Wundke, K. *et al.* PbS quantum-dot-doped glasses for ultrashort-pulse generation. *Appl. Phys. Lett.* **76**, 10–12 (2000).
16. Sasaki, A. *et al.* Recombinant protein (EGFP-Protein G)-coated PbS quantum dots for in vitro and in vivo dual fluorescence (visible and second-NIR) imaging of breast tumors. *Nanoscale* **7**, 5115–5119 (2015).
17. Onwudiwe, D. Microwave-assisted synthesis of PbS nanostructures. *Heliyon* **5**, e01413 (2019).
18. Zhang, Z., Lee, S., Vittal, J. & Chin, W. A simple way to prepare PbS nanocrystals with morphology tuning at room temperature. *J. Phys. Chem. B* **110**, 6649–6654 (2006).
19. Yu, D., Wang, D., Meng, Z., Lu, J. & Qian, Y. Synthesis of closed PbS nanowires with regular geometric morphologies. *J. Mater. Chem.* **12**, 403–405 (2002).
20. Lee, S., Jun, Y., Cho, S. & Cheon, J. Single-crystalline star-shaped nanocrystals and their evolution: Programming the geometry of nano-building blocks. *J. Am. Chem. Soc.* **124**, 11244–11245 (2002).
21. Singh, K., McLachlan, A. & Marangoni, D. Effect of morphology and concentration on capping ability of surfactant in shape controlled synthesis of PbS nano- and micro-crystals. *Colloids Surf. A Physicochem. Eng. Asp.* **345**, 82–87 (2009).
22. Pendyala, N. & Rao, K. Temperature and capping dependence of NIR emission from PbS nano-micro-crystallites with different morphologies. *Mater. Chem. Phys.* **113**, 456–461 (2009).
23. Borhade, A., Uphade, B. & Tope, D. Synthesis, characterization, and catalytic application of PbS nanoparticles for the synthesis of amidoalkyl naphthols under solvent-free conditions. *Res. Chem. Intermed.* **40**, 211–223 (2014).
24. Babu, R., Kumar, J., Bai, S., Singh, J. & Reddy, V. Carboxymethyl cellulose stabilized lead sulfide nanocrystals: Synthesis, characterization and catalytic applications. *Colloids Surf. A Physicochem. Eng. Asp.* **620**, 126572–126580 (2021).
25. Ajibade, P. & Oluwalana, A. Synthesis and crystal structureof bis (*o*-methyl hydrogenato carbonodithioate)-Pb(II): Structural, optical and photocatalytic studies of PbS nanoparticles from thecomplex. *J. Coord. Chem.* **72**, 3575–3588 (2019).
26. Oluwalana, A. & Ajibade, P. Structural, optical and photocatalytic studiesof hexadecylamine-capped lead sulfide nanoparticles. *Int. J. Ind. Chem.* **11**, 2490–3260 (2020).
27. Nugraha, M. *et al.* Enabling ambipolar to heavy n-type transport in PbS Quantum dot solids through doping with organic molecules. *ACS Appl. Mater. Interfaces* **9**, 18039–18045 (2017).
28. Balazs, D. *et al*. Stoichiometric control of the density of states in PbS colloidal quantum dot solids. *Sci. Adv*. **3**, eaao1558 (2017).
29. Koh, W. *et al.* Heavily doped n-type PbSe and PbS nanocrystals using ground-state charge transfer from cobaltocene. *Sci. Rep.* **3**, 1–8 (2014).
30. Ushakova, E. *et al.* 3D structures with an orthorhombic lattice assembled by collodial PbS quantum dot. *Nanoscale* **10**, 8313–8320 (2008).
31. Khan, A. *et al.* Solution-processed free-standing ultrathin two-dimensional pbs nanocrystals with efficient and highly stable dielectric properties. *Chem. Mater.* **29**, 1175–1182 (2017).
32. Jana, S., Thapa, R., Maity, R. & Chattopadhyay, K. Optical and dielectric properties of PVA capped nanocrystalline PbS thin films synthesized by chemical bath deposition. *Phy. E: Low-Dimens. Syst. Nanostruct.* **40**, 3121–3126 (2008).
33. Shkir, M., Khan, A., Hamdy, M. & Alfaify, S. A facile microwave synthesis of PbS: Sr nanoparticles and their key structural, morphological, optical, photoluminescence, dielectric and electrical studies for optoelectronics. *Mater. Res. Express* **6**, 1250e6 (2019).
34. Shkir, M. *et al.* Enhanced dielectric and electrical properties of PbS nanostructures facilely synthesized by low-cost chemical route: An effect of Ce-doping concentrations. *Mater. Chem. Phys.* **278**, 125626 (2022).
35. Afsar, M., Jamil, A. & Rafiq, M. Ferroelectric, dielectric and electrical behavior of two-dimensional lead sulphide nanosheets. *Adv. Nat. Sci.: Nanosci. Nanotechnol.* **8**, 045010 (2017).
36. Onoda, M., Kato, K., Gotoh, Y. & Osawa, Y. Structure of the incommensurate composite crystal $(PbS)_{1.12}VS_2$. *Acta Cryst.* **B46**, 487–492 (1990).
37. Grzechnik, A. & Friese, K. Pressure-induced orthorhombic structure of PbS. *J. Phys.: Condens. Matter* **22**, 095402 (2010).
38. Zagorac, D., Doll, K., Schon, J. & Jansen, M. Ab initio structure prediction for lead sulfide at standard and elevated pressures. *Phys. Rev. B* **84**, 045206 (2011).
39. Contreras, R. J., Díaz, R. J., Luna, S. S., Carrillo, T. R. & Sánchez, Z. R. Characterisation of chemical bath deposition PbS nano films using polyethyleneimine, triethanolamine and ammonium nitrate as complexing agents. *Thin Solid Films* **692**, 137609 (2019).
40. Sadovnikova, S., Vovkotrub, E. & Rempel, A. Micro-Raman spectroscopy of nanostructured silver sulfide. *Dokl. Phys. Chem.* **480**, 81–84 (2018).
41. Turcotte, S. *et al.* Application of Raman spectroscopy to metal-sulfide surface analysis. *Appl. Opt.* **32**, 935–938 (1993).
42. Pinilla, D. *et al.* Morphology and band structure of orthorhombic PbS nanoplatelets: An indirect band gap material. *Chem. Mater.* **33**, 420–429 (2021).
43. Cao, H., Wang, G., Zhang, S. & Zhang, X. Growth and photoluminescence properties PbS nanocubes. *Nanotechnology* **17**, 3280–3287 (2006).
44. Akhtar, J. *et al.* A greener route to photoelectrochemically active PbS nanoparticles. *J Mater. Chem.* **20**, 2336–2344 (2010).
45. Ivanov, A., Nebogatikova, N., Kotin, I. & Antonova, I. Two-layer and composite films based on oxidized and fluorinated graphene. *Phys. Chem. Chem. Phys.* **19**, 19010–19020 (2017).
46. Koaib, J. *et al*. Dielectric and electrical properties of annealed ZnS thin films. The appearance of the OLPT conduction mechanism in chalcogenides. *RSC Adv*. **10**, 9549–9562 (2020).
47. Ghosh, S., Perla, V. & Mallick, K. Organic molecule stabilized bismuth iodide nanoparticle: A hybrid system with multifunctional physical properties. *Phys. Chem. Chem. Phys.* **22**, 1–7 (2019).
48. Li, T. *et al.* Integrated molecular diode as 10 MHz half-wave rectifier based on an organic nanostructure heterojunction. *Nat. Commun.* **11**, 3592 (2020).
49. Grobosch, M. & Knupfer, M. Charge-injection barriers at realistic metal-organic interfaces: Metals become faceless. *Adv. Mater.* **19**, 754–756 (2007).
50. Elliot, S.R. A.C. conduction in amorphous chalcogenide and pnictide semiconductors. *Adv. Phys*., **36**, 135–217 (1987).
51. Chen, G. *et al.* Improved of dielectric performance and temperature-dependent behaviour of polyvinylidene fluoride composite with $KTa_{0.5}Nb_{0.5}O_3$@Ag nanoparticles. *J. Phys. Chem. C* **121**, 15028–15035 (2017).
52. Ranesan, M. T. Synthesis, characterization, and properties of new conducting polyaniline/copper sulfide nanocomposite. *Polym. Eng. Sci.* **54**, 438–445 (2014).
53. Meloni, S. *et al.* Ionic polarization-induced current-voltage hysteresis in $CH_3NH_3PbX_3$ perovskite solar cell. *Nat. Commun.* **7**, 10334 (2016).
54. Li, J., Li, F. & Zhang, S. Decoding the fingerprint of ferroelectric loops: Comprehension of the material propeprties and strucutres. *J. Am. Ceram. Soc.* **97**, 1–27 (2014).
55. Lemsi, A. *et al.* Lead sulfide nanocubes for solar energy storage. *Energy Technol.* **8**, 2000301 (2020).
56. Lin, W. *et al.* Highly luminescent lead sulfide nanocrystals in organic solvents and water through ligand exchange with poly(acrylic acid). *Langmuir* **24**, 8215–8219 (2008).
57. Watt, A. *et al.* Lead sulfide nanocrystal: conducting polymer solar cells. *J. Phys. D: Appl. Phys.* **38**, 2006–2012 (2006).

58. Khan, A. *et al.* Evolution of long range bandgap tunable lead sulfide nanocrystals with photovoltaic properties. *J. Phys. Chem. C* **117**, 7934–7939 (2013).
59. Ghamsari, M., Ara, M., Radimanc, S. & Zhang, X. Colloidal lead sulfide nanocrystals with strong green emission. *J. Lumin.* **137**, 241–244 (2013).
60. Roshan, H., Sheikhi, M., Haghighi, M. & Padidar, P. High-performance room temperature methane gas sensor based on lead sulfide/reduced graphene oxide nanocomposite. *IEEE Sens. J.* **20**, 2526–2532 (2020).
61. Akkerman, Q. *et al.* Ultrathin orthorhombic PbS nanosheets. *Chem. Mater.* **31**, 8145–8153 (2019).

Acknowledgements

This study was financially supported by the Faculty of Science, University of Johannesburg. Centre for Material Analysis, University of Oulu, Finland, is also acknowledged for XPS characterizations. We also acknowledge Professor Wei Cao from University of Oulu for his comments.

Author contributions

S.G. and K.M. developed and designed the concept. S.G. executed the methodology. Computational analysis was performed by M.O. H.S. was involved in XPS measurement and data discussion. Material characterization was done by I.W., and R.U.I. All of the authors have read and agreed to the final version of the manuscript. K.M. directed the research.

Competing interests

The authors declare no competing interests.

Additional information

Supplementary Information The online version contains supplementary material available at https://doi.org/10.1038/s41598-022-23909-z.

Correspondence and requests for materials should be addressed to K.M.

Reprints and permissions information is available at www.nature.com/reprints.

Publisher's note Springer Nature remains neutral with regard to jurisdictional claims in published maps and institutional affiliations.